Supporting Information

Csanády et al. 10.1073/pnas.0911061107

SI Text

Comparing Strategies for Choosing t_{crit} for Burst Analysis. Because the durations of intra- and interburst closures overlap, the true sequence of open bursts cannot be flawlessly reconstructed; regardless of the choice of t_{crit}, there will be a fraction of interburst closures shorter than t_{crit} (these will be erroneously discarded) and a fraction of intraburst closures longer than t_{crit} (these will be retained and mistakenly treated as interburst closures). Two strategies for choosing t_{crit} are (*i*) to minimize the total number of misclassified closures (1) or (*ii*) to equalize the numbers of misclassified intra- and interburst closures (2). Because the inevitable distortion of the true burst distributions by these two (and other) procedures have not yet been studied, we used large simulated data sets to evaluate this distortion for methods (*i*) and (*ii*), when applied to a single-exponential burst distribution (Fig. S1) and to a peaked burst distribution resulting from a nonequilibrium mechanism (Fig. S2). As expected, our analysis found method (*i*) slightly more accurate for extracting the average length of single exponentially distributed bursts (Fig. S1). However, we found that method (*ii*) caused less overall distortion of burst distributions, and consequently produced more accurate rate estimates for an irreversible cyclic mechanism similar to scheme 2 of this paper (Fig. S2). The relative accuracy of the two methods in preserving the shapes of burst duration distributions is likely to depend on the particular models and the values of their rate constants. It is therefore recommended that an evaluation similar to that described here be undertaken for each case.

Defining the Durations of ATP-Driven Open Bursts for WT and Mutant CFTR Channels. Opening of CFTR channels from an interburst closure requires binding of ATP, as reflected by the [ATP] dependence of the mean interburst (but not intraburst) duration (τ_{ib}) (3, 4). In contrast, the lack of [ATP] dependence of the microscopic mean open burst duration (τ_b) shows that once open, a CFTR channel can proceed through a burst of openings without further ATP binding (3–5). Consequently, the time constant of macroscopic current decay after sudden ATP removal from inside-out patches containing many CFTR channels is identical to the microscopic τ_b (5, 6) (Fig. S3*A*), so providing an alternative way to estimate burst length.

In this work we also examine the gating behavior of NBD1 Walker A mutant CFTR, K464A, and of NBD2 Walker B mutant CFTR, D1370N. As the pattern of steady-state gating may be more complex in catalytic site mutants (e.g., ref. 6), two types of information can aid assignment of a particular closed-time component as intra- or interburst. First, the predicted microscopic τ_b should match the time constant of macroscopic current decay upon ATP withdrawal, as described. Second, in such ATP-removal experiments, closed events can be collected from the periods of time during which only a single CFTR channel is left in the open bursting state before it too finally closes for good. The distribution of such closures—which must all be intraburst given the absence of ATP—can be compared with the closed-time distribution obtained from steady-state gating in ATP (6). For instance, D1370N CFTR (Fig. S3*C*) has a closed-time distribution in ATP with four discernible exponential components (Fig. S3*D*), the shortest two of which we could confidently assign as intraburst because (*i*) the time constant of macroscopic current decay following removal of ATP from patches containing many D1370N channels (Fig. S3*E*) matches the steady-state burst duration calculated assuming two intra- and two interburst components (Fig. S3*D*), and (*ii*) the closed-time distribution of the last open channel following removal of ATP (Fig. S3*E*, blue bar) contains two components (Fig. S3*F*) with time constants identical to those of the two briefest components of the steady-state closed-time distribution (Fig. S3*D*).

Systematic ML Evaluation of a Full Range of Models for Each Set of Data. ML fitting allows quantitative comparison of alternative gating models because it provides a numerical value for the "goodness" of a fit in the form of the log-likelihood (LL) score. When comparing two models with equal numbers of free parameters, the model that provides a higher LL value is ranked higher. Comparing models with different numbers of free parameters is more problematic, because more free parameters typically results in a higher LL value, even if introduction of the additional parameters is not justified. However, if the model with fewer parameters is a submodel of the other (the models are nested) and certain regularity criteria apply, the distribution of expected log-likelihood ratios ($\Delta LL = LL_2\text{-}LL_1$) can be calculated and compared with the observed value of ΔLL (ΔLL_{obs}). In such cases, the two models can be ranked using the LL ratio test. Thus, for a given significance level P (e.g., 0.05, 0.01, etc.), the larger model is ranked higher if $\int_{\Delta LL_{obs}}^{\infty} h(x)dx < P$ holds [$h(x)$ is the expected pdf of ΔLL values]; otherwise, the submodel is ranked higher.

Using this methodology, we systematically ranked two linear and four cyclic models (Fig. S4*A*; free parameters are depicted in red) for their ability to account for the four datasets described in this paper, i.e., the distributions of burst durations of fully phosphorylated WT, and partially phosphorylated WT, K464A, and D1370N CFTR channels. Schemes 1 and 2 are identical to those shown in Fig. 1*A* except that, for purposes of studying open bursts, the two closed states C_1 and C_2 in Fig. 1*A* are merged here into compound state C. In schemes 2a and 2b (Fig. S4*A*), rate k_{-1} is fixed either to zero (cf. Figs. 1*B* and 3*B*) or to the rate of nonhydrolytic closure of WT CFTR estimated from the closing rate of the K1250R mutant (Fig. 4*E Right*, blue bar). Scheme 3 is a generalization of scheme 2a in which the $O_1 \rightarrow O_2$ step is allowed to be reversible. Finally, scheme 4 is a two-component equilibrium model used for fitting the D1370N data in Fig. 1*C*. Using the notation A⊂B to denote that model A is nested in model B, the following relationships hold between the six schemes shown: 1⊂2a⊂2, 1⊂2b⊂2, 2a⊂3, 1⊂4. Importantly, for each of these relationships the distributions of ΔLL values for the case that the submodel is true have been either calculated or empirically determined (7), thereby justifying the use of the LL ratio test.

Because in a two-open-state model, the open-time pdf is described by only three parameters (two time constants plus a fractional amplitude), models with more than three free parameters are not identifiable by ML fitting. Not only are such models poorly defined (i.e., an infinite set of parameter vectors yield identical pdfs), but the distributions of ΔLL values are also unknown, precluding interpretation of the obtained LL ratio in terms of statistical significance. We could therefore not evaluate cyclic models in which more than one step is made reversible at a time. Nor did we include a cyclic model in which step $C \rightarrow O_2$ is made reversible, because (*i*) we and others have shown that ADP (or ADP+phosphate) does not open CFTR channels, even when applied at high millimolar concentrations (8), and (*ii*) because in our experiments both ADP and phosphate concentrations were

kept at nominally zero levels by a continuously and rapidly flowing ADP- and phosphate-free bath solution.

Fig. S4*B* summarizes the LL values obtained for fitting the four data sets to each of the schemes in Fig. S4*A* (relative to the LL value obtained for scheme 1), and Fig. S4*C* illustrates the rankings between the models based on the LL ratio test using $P = 0.05$. These rankings, based solely on the LL scores, largely confirm our conclusions discussed for the four data sets in the main text. Notably, for all four data sets, scheme 3 ranked lower than scheme 2a, suggesting that the ATP-hydrolysis step itself is indeed irreversible, and supporting our choice of scheme 2 as a framework to interpret our data. Two ranking decisions need further support from independent observations.

For D1370N, schemes 2 and 4 (Fig. S4) are ranked equal, as both schemes are capable of producing two positive-amplitude exponential components. However, the fit with scheme 2 yields rate estimates ($k_{-1} = 0.78\ s^{-1}$; $k_1 = 4.27\ s^{-1}$; $k_2 = 0.49\ s^{-1}$) that are incompatible with the functional interpretation of the steps in scheme 2 and known consequences of the D-to-N mutation of the Walker B aspartate in ABC proteins (see main text for references). That is, this fit would suggest a high coupling ratio of 85% with essentially intact ATP hydrolysis, whereas the mutation is known to abrogate ATP hydrolysis in ABC proteins. Further, based on the extremely slow rate k_2 yielded by this fit, the mutation would have to stabilize the posthydrolytic NBD dimer by ~100-fold, although it is known to destabilize the dimer due to impaired Mg^{2+} binding. We therefore consider the equilibrium scheme 4 the best model for describing the gating of D1370N (see *Discussion* in main text).

For partially phosphorylated WT CFTR—but not for fully phosphorylated WT—leaving k_{-1} as a free parameter in scheme 2 resulted in a small but significant improvement ($\Delta LL = 3.83$; $P = 6{\cdot}10^{-3}$) relative to fixing it to the rate estimate shown in Fig. 4*E Right* (blue bar). Though still predicting a highly nonequilibrium mechanism, the three-parameter fit ($k_{-1} = 1.82\ s^{-1}$; $k_1 = 2.70\ s^{-1}$; $k_2 = 23.4\ s^{-1}$) yielded a lower coupling ratio (60%) for partially phosphorylated WT than the one shown in Fig. 4*F* (95%). However, several independent observations lead us to question the reliability of these rate estimates. First, the large value of $1.82\ s^{-1}$ for rate k_{-1} is inconsistent with the slow closing rate invariably observed for several NBD2 mutants in which ATP hydrolysis is disrupted (K1250A, K1250R, E1371S), or for WT CFTR locked in the open state by nonhydrolyzable ATP analogs (e.g., AMP-PNP). Second, taken at face value, the rankings in Fig. S4*C* would suggest that k_{-1} for WT increases by ~8-fold upon removal of PKA. Though the rapid partial dephosphorylation prevents us from rigorously measuring closing rates of fully phosphorylated nonhydrolytic mutants (Fig. 2*A*), there is at least no evidence for a major change in this rate upon partial dephosphorylation. For example, nucleotide removal from K1250R channels opened by 300 nM PKA + 2 mM ATP results in a macroscopic closing rate [0.22 ± 0.004 ($n = 8$)] indistinguishable from the one obtained for channels opened by just 2 mM ATP [0.22 ± 0.01 ($n = 17$)]. Third, the ML fitting assumes an ideal, homogeneous data set with rates that remain constant throughout the experiment. Because of the slow gating of CFTR, we had to fit pooled data collected from several single-channel patches to obtain sufficient numbers of burst events. For example, the data for partially phosphorylated WT were pooled from 20 patches. When we subdivided this data into subsets, the improvement by scheme 2 relative to 2b was not consistently present in all subsets, suggesting data inhomogeneity. To test the effect of such inhomogeneity on the fitting, we simulated 1,000 bursts using scheme 2a with rates $k_1 = 4\ s^{-1}$, $k_2 = 30\ s^{-1}$, and 1,000 bursts using the same scheme but rates $k_1 = 4\ s^{-1}$, $k_2 = 50\ s^{-1}$, and then merged the two data sets. Fitting the pooled data with scheme 2a resulted in rate estimates $k_1 = 3.92\ s^{-1}$, $k_2 = 47.6\ s^{-1}$, together with a large improvement relative to scheme 1 ($\Delta LL = 21.00$; $P = 9{\cdot}10^{-11}$). Interestingly, though scheme 2b fitted only slightly better than 2a ($\Delta LL = 0.51$), scheme 2 fitted significantly better ($\Delta LL = 3.14$; $P = 0.01$), yielding rate estimates ($k_{-1} = 1.83\ s^{-1}$; $k_1 = 2.32\ s^{-1}$; $k_2 = 17.3\ s^{-1}$) similar to those we obtained for fitting our experimental data for partially phosphorylated WT. Taking these limitations into account, we consider scheme 2b (Fig. S4) as the best approximation of the mechanism of gating of both fully and partially phosphorylated WT CFTR.

1. Jackson MB, Wong BS, Morris CE, Lecar H, Christian CN (1983) Successive openings of the same acetylcholine receptor channel are correlated in open time. *Biophys J* 42:109–114.
2. Magleby KL, Pallotta BS (1983) Burst kinetics of single calcium-activated potassium channels in cultured rat muscle. *J Physiol* 344:605–623.
3. Winter MC, Sheppard DN, Carson MR, Welsh MJ (1994) Effect of ATP concentration on CFTR Cl- channels: A kinetic analysis of channel regulation. *Biophys J* 66:1398–1403.
4. Vergani P, Nairn AC, Gadsby DC (2003) On the mechanism of MgATP-dependent gating of CFTR Cl- channels. *J Gen Physiol* 121:17–36.
5. Csanády L, et al. (2000) Severed channels probe regulation of gating of cystic fibrosis transmembrane conductance regulator by its cytoplasmic domains. *J Gen Physiol* 116:477–500.
6. Bompadre SG, et al. (2005) CFTR gating II: Effects of nucleotide binding on the stability of open states. *J Gen Physiol* 125:377–394.
7. Csanády L (2006) Statistical evaluation of ion-channel gating models based on distributions of log-likelihood ratios. *Biophys J* 90:3523–3545.
8. Csanády L, Nairn AC, Gadsby DC (2006) Thermodynamics of CFTR channel gating: A spreading conformational change initiates an irreversible gating cycle. *J Gen Physiol* 128:523–533.

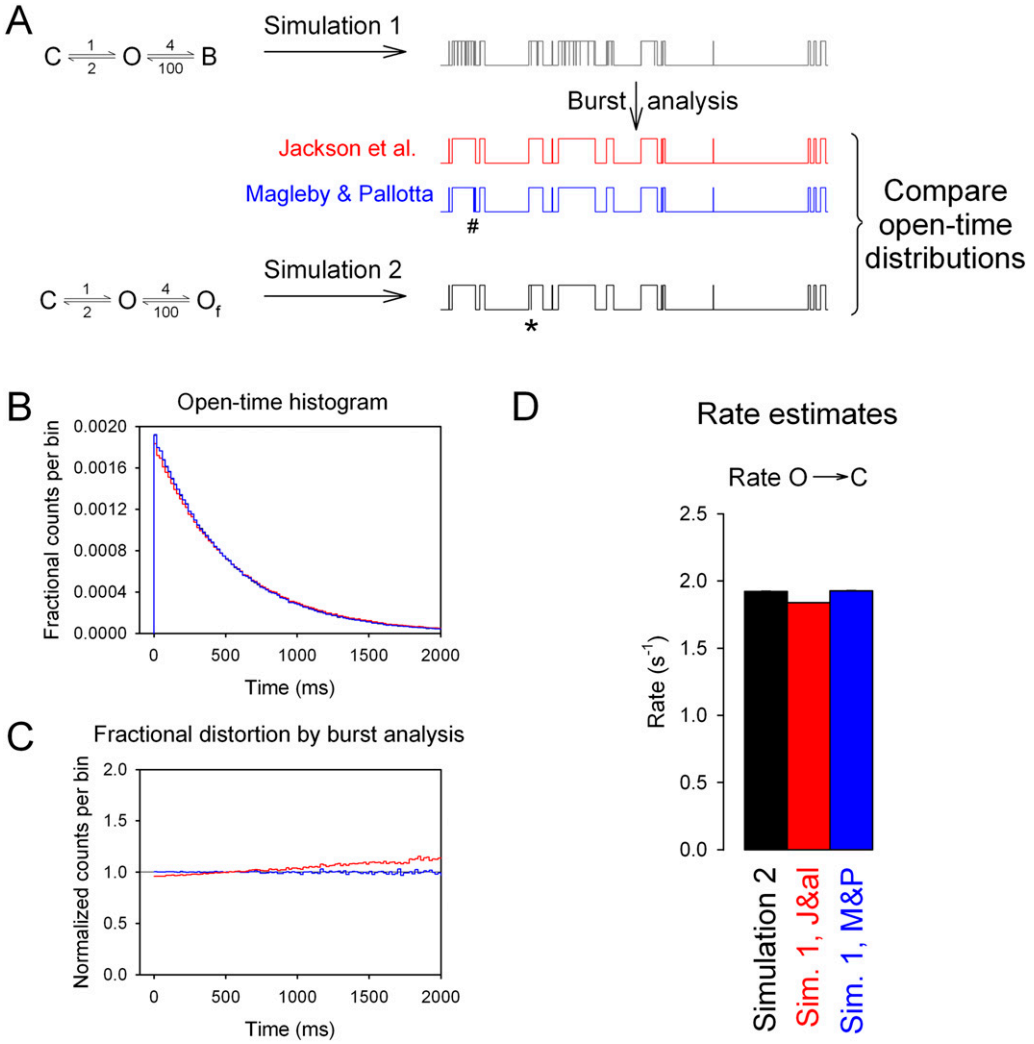

Fig. S1. Distortion of an essentially single-exponential burst distribution by two alternative burst analysis strategies. (*A*) 6×10^6 events were simulated using the closed (C) - open (O) - blocked (B) scheme (*Top Left*; rates, in s^{-1}, are printed on the scheme), and the resulting sequence of events (*Top Right*, gray trace illustrates a 20-s segment) subjected to burst analysis using either the method of Jackson et al. (1) (method *i*) or that of Magleby and Pallotta (2) (method *ii*), to reconstruct two tentative sequences of bursts (*Center Right*, red and blue traces). As a control, the true sequence of bursts (*Bottom Right*, black trace) for this mechanism was obtained by simulating 6×10^6 events using a gating scheme (*Bottom Left*) in which the brief (intraburst) closed-state B was replaced by a conducting state (O_f), whereas the rate constants and the seed value for the random sequence generator remained unchanged. Note one interburst closure (*) erroneously eliminated in both reconstructed traces, and one intraburst closure (#) mistakenly classified as interburst using method (*ii*). (*B*) Open-time histograms constructed from the true sequence (black) and the two reconstructed sequences of events (red, blue), all three normalized to integrate to unity. All three distributions are essentially single exponential; the black and the blue traces overlap. (*C*) Evaluation of the fractional distortions of the true burst distribution by strategies (*i*) and (*ii*). Each bincount of the red and blue open-time histograms in (*B*) was divided by the corresponding bincount of the true (black) open-time histogram, to yield histograms of fractional distortion (red and blue histograms in *C*). Because method (*ii*) equalizes the numbers of misclassified intra- and interburst closures, it causes no distortion to a single-exponential burst distribution. (*D*) Estimates of the rate of closing from a burst, obtained by fitting the true sequence (black bar) and the two reconstructed sequences of bursts (red and blue bars) by a C-O scheme using ML. Error bars are 0.5-unit log-likelihood intervals, but are too small to be seen. Method (*ii*) returns an unbiased estimate.

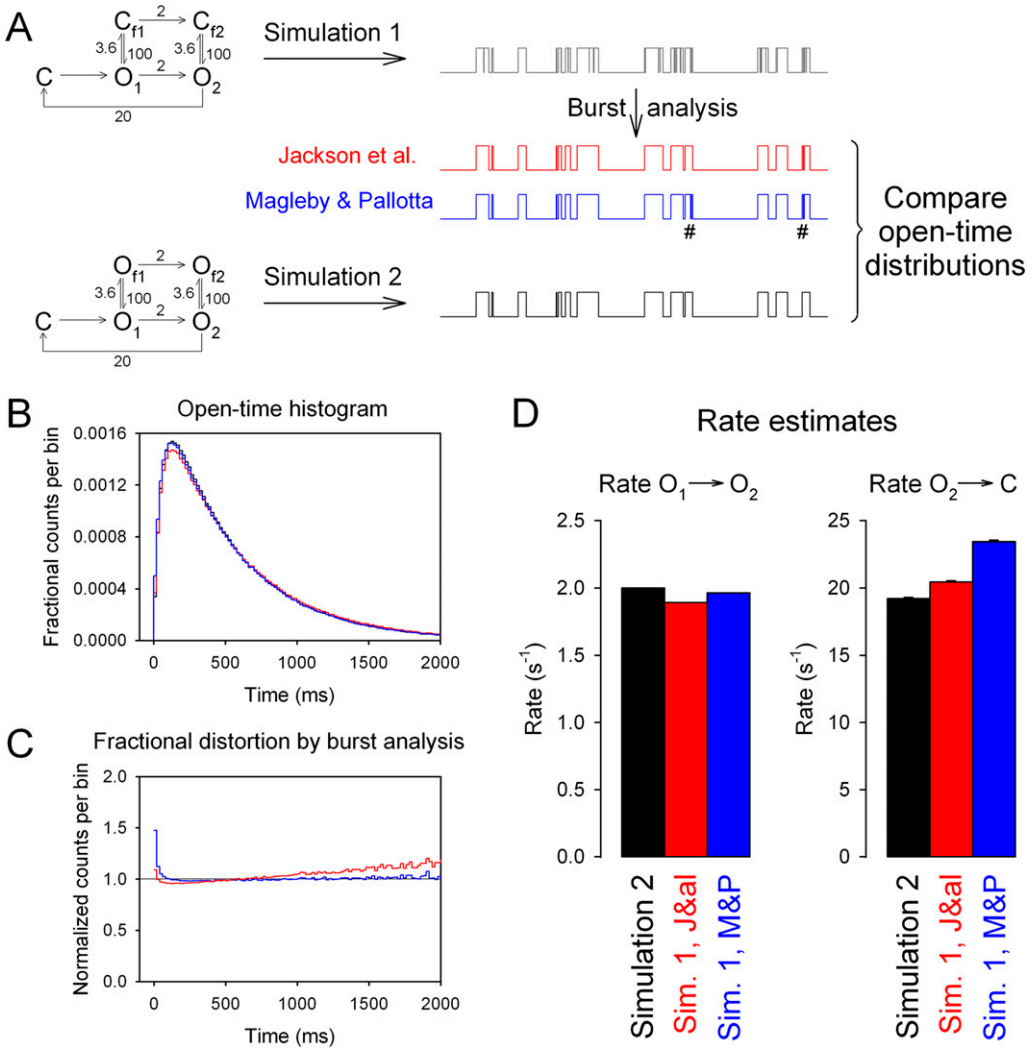

Fig. S2. Distortion of the burst distribution of a cyclic mechanism by two alternative burst analysis strategies. (*A*) 7×10^6 events were simulated using a cyclic mechanism (*Top Left*; rates are printed on the scheme) such as scheme 2 with $k_{-1} = 0$ (Fig. 1*A*), supplemented with brief intraburst closed states (C_{f1}, C_{f2}). (For the purpose of studying open bursts, the two closed states C_1 and C_2 in scheme 2 are merged here into a single state C.) The resulting sequence of events (*Top Right*, gray trace illustrates a 20-s segment) was subjected to burst analysis using method (*i*) or (*ii*) (see *Methods*) to reconstruct two tentative sequences of bursts (*Center Right*, red and blue traces). As a control, the true sequence of bursts (*Bottom Right*, black trace) for this mechanism was obtained by simulating 7×10^6 events using a gating scheme (*Bottom Left*) in which the brief (intraburst) closed states C_{f1} and C_{f2} were replaced by conducting states (O_{f1}, O_{f2}), whereas the rate constants and the seed value for the random sequence generator remained unchanged. Note two intraburst closures (#) erroneously misclassified as interburst using method (*ii*), the second of them also misclassified using method (*i*). (*B*) Open-time histograms constructed from the true sequence (black) and the two reconstructed sequences of events (red, blue), all normalized to integrate to unity. (*C*) Evaluation of the fractional distortions of the true burst distribution by methods (*i*) and (*ii*). Each bincount of the red and blue open-time histograms in (*B*) was divided by the corresponding bincount of the true (black) open-time histogram, to yield histograms of fractional distortion (red and blue histograms in *C*). (*D*) Estimates of the rates $O_1 \rightarrow O_2$ (*Left*) and $O_2 \rightarrow C$ (*Right*) obtained by fitting the true sequence (black bars) and the two reconstructed sequences of bursts (red and blue bars) by scheme 2 with k_{-1} fixed to zero, using ML. Barely visible error bars are 0.5-unit log-likelihood intervals. Note that, overall, method (*i*) causes less distortion (*C*) and provides more accurate rate estimates (*D*) for this mechanism.

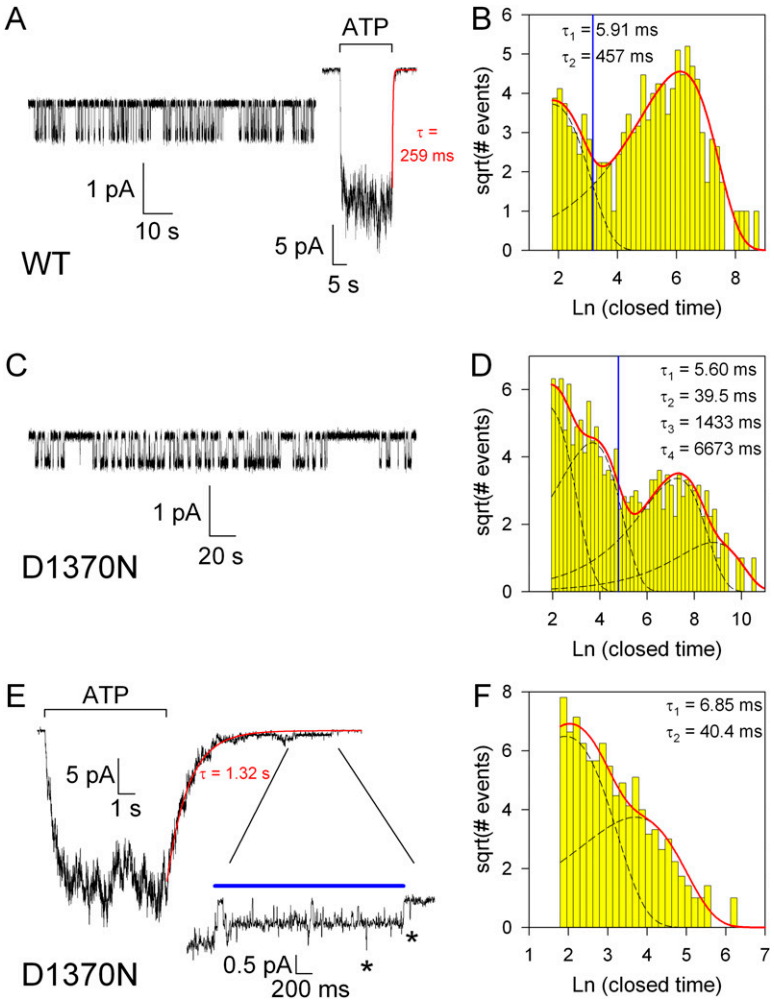

Fig. S3. Defining ATP-dependent bursts for WT and D1370N CFTR. (*A*) Current trace from a single prephosphorylated WT CFTR channel gating at steady state in 2 mM ATP (*Left*) and macroscopic current response (*Right*) of >100 prephosphorylated WT CFTR channels to a brief exposure (bar) to 2 mM ATP. The red line is a single-exponential fit to the current decay time course following ATP removal, yielding a time constant of 259 ms. (*B*) Closed-time histogram pooled from two single-channel records including the one shown in (*A*). The red line is a ML fit by a mixture of two exponentials; individual components are depicted by dashed lines, and time constants are indicated. (The third long component with vanishing fractional amplitude apparent in the histogram was not typically observed.) The blue line depicts t_{crit} using method (*i*) and assuming one intra- and one interburst component. Using this t_{crit}, burst analysis of this set of data yielded a mean burst duration of 278 ms. (*C*) Current trace from a single prephosphorylated D1370N CFTR channel gating at steady state in 2 mM ATP. (*D*) Closed-time histogram pooled from four single-channel records, including the one shown in (*C*). The red line is a ML fit by a mixture of four exponentials; individual components are depicted by dashed lines, and time constants are indicated. Burst analysis (using method *ii*) based on assigning 1, 2, or 3 components as intraburst yielded mean burst durations of 518 ms, 1,324 ms, and 12.4 s, respectively; the blue line depicts t_{crit} using method (*ii*) and assuming two intraburst components. (*E*) Macroscopic current response of ~100 prephosphorylated D1370N CFTR channels to a brief exposure (bar) to 2 mM ATP. The red line is a single-exponential fit to the current decay time course following ATP removal, yielding a time constant τ = 1.32 s; average τ was 1.4 ± 0.1 s (n = 3). Asterisks mark infrequent brief spontaneous openings in the absence of ATP. (*F*) Dwell-time histogram of intraburst closures collected from stretches of record in which only one D1370N channel has remained in the bursting state following ATP removal (see *E Inset*, period marked by blue bar). Closed events before the final closure (these must be intraburst given the lack of ATP in the bath) were pooled from 34 experiments. The red line is a ML fit by a mixture of two exponentials; individual components are depicted by dashed lines, and time constants are indicated. Note that these time constants are similar to those of the two briefest components of the steady-state closed-time distribution (Fig. S3*D*).

A

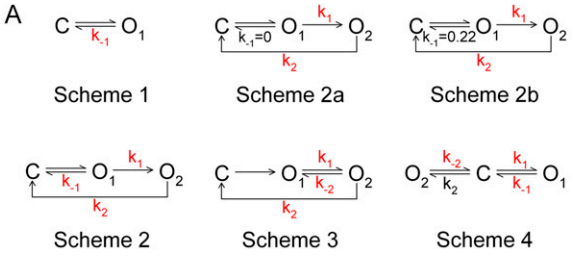

B

	Sch. 4	Sch. 1	Sch. 2a	Sch. 3	Sch. 2b	Sch. 2
WT+PKA	0.00	0	17.34	17.34	19.03	20.26
WT	0.00	0	18.01	18.01	18.83	22.66
K464A	0.00	0	0.00	0.00	0.00	3.62
D1370N	3.24	0	0.00	0.00	0.00	3.24

C

WT+PKA: Sch. 4 < Sch. 1 << Sch. 3 < Sch. 2a < Sch. 2 < Sch. 2b

WT: Sch. 4 < Sch. 1 << Sch. 3 < Sch. 2a < Sch. 2b < Sch. 2

K464A: Sch. 4 < Sch. 3 < Sch. 2a = Sch 2b < Sch. 1 < Sch. 2

D1370N: Sch. 3 < Sch. 2a = Sch 2b < Sch. 1 < Sch. 2 = Sch. 4

Fig. S4. Comprehensive summary of ML fitting results. (*A*) Two linear equilibrium and four cyclic nonequilibrium models were tested for their ability to describe the distributions of burst durations. Free parameters are shown in red. (*B*) Summary of LL values obtained for fitting the six schemes in (*A*) to the distributions of burst durations of fully phosphorylated WT, and of partially phosphorylated WT, K464A, and D1370N CFTR channels. LL values are presented relative to that obtained for fitting the same data set with scheme 1 (i.e., for scheme *n*, LL(*n*) – LL(1) is shown). (*C*) Rankings of the six schemes in (*A*) for each of the four data sets, obtained using the LL ratio test with $P = 0.05$. The highest ranked model appears on the right.